PCCP

ROYAL SOCIETY OF CHEMISTRY

PAPER

View Article Online
View Journal | View Issue

Check for updates

Cite this: *Phys. Chem. Chem. Phys.*, 2025, **27**, 24381

Received 9th October 2025,
Accepted 28th October 2025

DOI: 10.1039/d5cp04123f

rsc.li/pccp

Probing the electronic structure and dipole-bound state of the 7-azaindolide anion

Jisoo Kang, Edward I. Brewer and Lai-Sheng Wang *

We report an investigation of the electronic structure and dipole-bound state (DBS) of the cryogenically-cooled 7-azaindolide anion (7-AI$^-$) using high-resolution photoelectron imaging, photodetachment spectroscopy, and resonant photoelectron spectroscopy. The electron affinity of the 7-AI radical is measured to be 2.6967(8) eV (21 751 ± 6 cm^{-1}). Two excited electronic states of the neutral radical are observed at 0.8 eV and 1.4 eV above the ground state. Two minor isomers of 7-AI$^-$ due to deprotonation from the α- and β-carbon on the pyrrole ring are also detected with lower adiabatic detachment energies. A DBS is observed for the 7-AI$^-$ anion at 156 cm^{-1} below the detachment threshold, along with 16 vibrational Feshbach resonances. Resonant two-photon photoelectron imaging reveals that the DBS is relatively long-lived. Resonant photoelectron spectroscopy *via* the vibrational Feshbach resonances of the DBS gives rise to rich vibrational features for the 7-AI radical not accessible in conventional photoelectron spectroscopy. Fundamental vibrational frequencies for 16 vibrational modes of the 7-AI neutral radical are measured experimentally, including 7 bending modes. The current work provides extensive experimental electronic and vibrational information for the 7-AI$^-$ anion and the 7-AI radical.

1. Introduction

The 7-azaindole molecule, its photophysics, and electronic structure have attracted significant research interest, because the dimer of 7-azaindole involves double H-bonds and is considered to be an ideal model system for the base pairs in the double-stranded DNA.[1–14] In particular, the excited-state double proton transfer in the 7-azaindole dimer has been investigated to gain insight into the stability and dynamics of the DNA base pairs.[15–25] In the two-step model for the double proton transfer, the intermediate consists of an ion pair, in which a proton is transferred from one 7-azaindole molecule to the other, leaving behind a deprotonated 7-azaindole anion (*i.e.* 7-azaindolide or 7-AI$^-$) and creating a protonated 7-azaindole cation. Thus, characterization of the 7-AI$^-$ anion is important for the understanding of the mechanisms of the double proton transfer in the 7-azaindole dimer. However, despite extensive investigations of the parent 7-azaindole molecule, there has been very little study on the 7-AI$^-$ anion or the 7-AI radical. Photoelectron spectroscopy (PES) and photodetachment spectroscopy (PDS) are the best techniques to characterize anions in the gas phase.[26] Indeed, the group of Lineberger first tried to study the 7-AI$^-$ anion using PES.[27] They measured a low resolution photoelectron (PE) spectrum at a photon energy of 3.494 eV, but their attempt to obtain high resolution PE spectra near threshold was not successful, because of the presence of vibrational hot bands and complicated autodetachment features attributed to the existence of a dipole-bound state (DBS). They were able to deduce an electron affinity (EA) of 2.699(1) eV for the 7-AI neutral radical.[27] More recently, Noble *et al.* reported a PDS study of the 7-AI$^-$ anion cooled in a cryogenic ion trap by detecting the neutral products.[28] They indeed observed a DBS at 160(10) cm^{-1} below the detachment threshold, as well as seven above-threshold vibrational levels of the DBS (a.k.a. vibrational Feshbach resonances). From the onset of the detachment threshold, Noble *et al.* obtained an EA of 21 750(10) cm^{-1} (2.697 eV) for the 7-AI radical, consistent with the preliminary value obtained by the Lineberger group.

High-resolution photoelectron imaging of cryogenically-cooled anions has been demonstrated to be a powerful technique to probe the electronic and vibrational structures of the corresponding neutrals.[29–32] We have shown that it is critical to conduct PDS on cryogenically-cooled anions to search for DBS.[32–35] In particular, we have developed resonant PES (rPES) *via* the vibrational Feshbach resonances, which can not only yield highly non-Franck Condon PE spectra with rich vibrational information inaccessible in conventional PES, but is also important to assist the assignment of the DBS vibrational features.[33,35–39] Combining PDS and rPES, we have investigated a number of complicated systems from simple aromatic anions to O-containing polycyclic aromatic hydrocarbon anions.[40–51] Using resonant two-photon detachment (R2PD) PES, we have also been able to deduce dynamical information about the bound DBS levels.[52–56]

Department of Chemistry, Brown University, Providence, RI 02912, USA.
E-mail: Lai-Sheng_Wang@brown.edu

In this study, we use this integrated spectroscopic strategy to probe the electronic structure and DBS of the 7-AI$^-$ anion and its corresponding 7-AI radical. High-resolution PE spectra yield an EA of 2.6967(8) eV (21 751 ± 6 cm^{-1}) for the 7-AI radical, while PES at high photon energies allows the observation of two low-lying excited electronic states for neutral 7-AI at 0.8 eV and 1.4 eV above its ground state. Two minor isomers due to deprotonation from the α- and β-carbon on the pyrrole ring are also detected at binding energies of 2.200(3) eV and 1.918(5) eV, respectively. A DBS is observed for the 7-AI$^-$ anion at 156(6) cm^{-1} below the detachment threshold, accompanied by 16 vibrational Feshbach resonances. R2PD PES *via* the zero-point level reveals that the DBS is relatively long-lived. The rPES *via* the 16 Feshbach resonances provides insights into the vibrational autodetachment processes and rich vibrational spectral features for the 7-AI neutral. The current study provides experimental values for 16 fundamental vibrational frequencies for the 7-AI radical, offering new electronic and spectroscopic benchmarks for further theoretical investigation of 7-AI$^-$ and its neutral counterpart.

2. Methods

2.1. Photoelectron imaging

The experiments were carried out using our home-built third-generation electrospray-ionization PES (ESI-PES) apparatus,[57] incorporating a cryogenic Paul trap and a high-resolution velocity-map imaging (VMI) system.[58–60] For the current study, the 7-AI$^-$ anions were produced *via* electrospray of a 1 mM solution of 7-azaindole (98%, Sigma-Aldrich) dissolved in a 9 : 1 methanol/water mixed solvent containing trace amount of NaOH to promote deprotonation. Anions from the ESI source were transported through a series of RF ion guides and subsequently accumulated and cooled in a Paul trap, which was maintained at 4.6 K using a closed-cycle helium refrigerator. Trapped ions are cooled by collisions with a 1 mTorr buffer gas consisting of a mixture of He/H$_2$ in a 4/1 volume ratio. After an accumulation and cooling period of ∼100 ms, the ions were pulsed out at a 10 Hz repetition rate into the extraction region of a time-of-flight mass spectrometer. The 7-AI$^-$ anion was mass-selected and photodetached in the VMI interaction zone using either a tunable dye laser or the third (3.496 eV) and fourth (4.661 eV) harmonics of an Nd:YAG laser. The resulting photoelectrons were mapped onto a pair of 75 mm microchannel plates coupled to a phosphor screen, and the spatially-resolved images were recorded using a CCD camera. Image reconstruction and angular integration were performed using the MELEXIR algorithm.[61] The energy scale was calibrated using the known PE spectrum of Au$^-$ at multiple photon energies. The system could achieve an energy resolution of ΔKE = 3.8 cm^{-1} at 55 cm^{-1}, with a relative resolution of ∼1.5% for electrons above 1 eV.[60] The VMI extraction voltages were adjusted to capture higher energy electrons and optimize image quality: −1200 V for the R2PD spectrum, −1000 V for the two PE spectra at 3.496 eV and 4.661 eV, −300 V for the rPES and the near-threshold PES.

2.2. Photoelectron angular distributions

VMI also provides photoelectron angular distributions (PAD), offering additional insight into the electronic characters of the detachment transitions. For randomly oriented molecules undergoing single-photon detachment by linearly polarized light, the differential cross section is given by:

$$\frac{d\sigma}{d\Omega} = \frac{\sigma_T}{4\pi} \cdot (1 + \beta P_2(\cos(\theta))), \quad (1)$$

where σ_T is the total cross section, P_2 is the second Legendre polynomial, θ is the angle relative to the laser polarization, and β is the anisotropy parameter. Thus, the PAD can be described by:

$$I(\theta) \sim (1 + \beta P_2(\cos(\theta))), \quad (2)$$

The β parameter ranges from −1 (perpendicular) to +2 (parallel).[62] In atomic systems, detachment from an s orbital (ℓ = 0) leads to p-wave (ℓ = 1) photoelectrons with β = 2, while detachment from a p-orbital (ℓ = 1) produces both s and d partial waves (ℓ = 0, 2) with β = −1. For molecular orbitals (MOs), the interpretation of the β parameter is more nuanced, but trends in β can still yield qualitative information about the orbital character of the electron being detached.

2.3. Computational methods

Theoretical calculations were conducted to help interpret the experimental observations. All calculations were performed using density functional theory (DFT) as implemented in Gaussian 09.[63] Ground-state geometries and harmonic vibrational frequencies of both the anion and the neutral species were calculated at the B3LYP/aug-cc-pVTZ level. Vertical detachment energies (VDEs) were computed using time-dependent DFT (TD-DFT) based on the optimized anion geometries. Franck–Condon (FC) factors were calculated with the FC-Lab2 program.[64]

3. Results

3.1. Non-resonant photoelectron imaging and spectroscopy

We first performed non-resonant PE imaging of the 7-AI$^-$ anion at 3.496 eV and 4.661 eV, as presented in Fig. 1. The 4.661 eV spectrum revealed three broad bands, X̃, Ã, and B̃. The 3.496 eV spectrum is dominated by vibrational features resolved for the X̃ band up to approximately 3.4 eV binding energy. The X̃ band arises from photodetachment transition to the ground electronic state of neutral 7-AI by removing an electron from the highest occupied molecular orbital (HOMO). Analysis of the PAD associated with band X̃ yields an anisotropy parameter of β = −0.40 ± 0.05, indicative of partial wave contributions beyond pure s-character, suggesting detachment from a π-type orbital, in agreement with the HOMO of 7-AI$^-$, as illustrated in Fig. 2. The most prominent transition at 2.7 eV defines the vibrational origin (0_0^0). The Ã band at ∼3.5 eV should be due to detachment

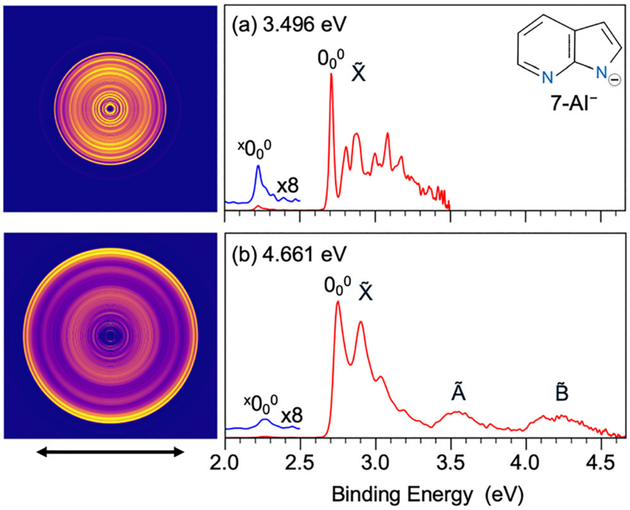

Fig. 1 Photoelectron images and spectra of the 7-AI$^-$ anion at (a) 3.496 eV and (b) 4.661 eV. The double arrow below the PE images indicates the polarization direction of the laser. The molecular structure of 7-AI$^-$ is shown as an inset in (a).

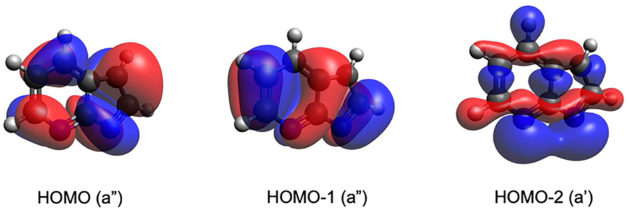

Fig. 2 The valence molecular orbitals of 7-AI$^-$.

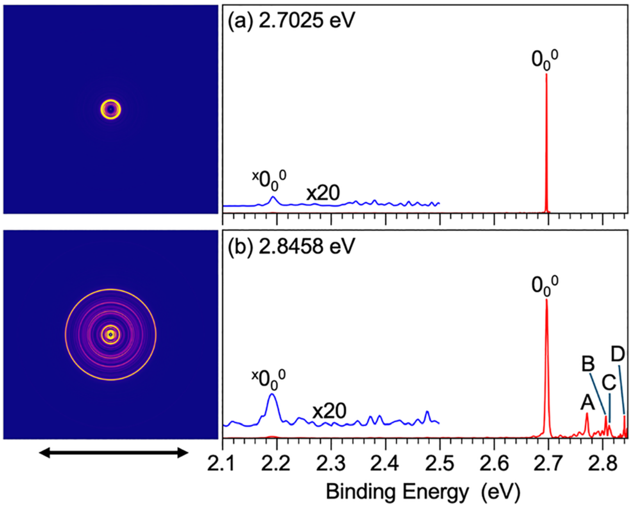

Fig. 3 High-resolution PE images and spectra of the 7-AI$^-$ anion at (a) 2.7025 eV (21 797 cm^{-1}) and (b) 2.8458 eV (22 953 cm^{-1}). The double arrow below the PE images indicates the laser polarization direction.

from the HOMO−1 of 7-AI$^-$, representing the first excited electronic state of neutral 7-AI. The HOMO−1 is also a π orbital, consistent with the β value (−0.28 ± 0.05) obtained from the PAD of band Ã. The broad band B̃ at ~4.1 eV should come from detachment from the HOMO−2 to the second excited state of the neutral molecule with a β value of −0.19 ± 0.05. The HOMO−2 is a delocalized σ orbital primarily formed by the in-plane p orbitals of C and N (Fig. 2). The PAD is clearly more isotropic and the β value is less conclusive in informing the electronic nature of the HOMO−2. We also computed the excitation energies of 7-AI, as compared with the experimental data in Table S1. We should note that a very weak feature is discernible on the low binding energy side at ~2.2 eV ($^{x}0_0^0$). As will be shown later, this signal arises from an isomer of 7-AI$^-$ (denoted as ^{x}7-AI$^-$), which is shown in Fig. S1.

We also obtained high-resolution PE images and spectra for the ground state detachment transition of 7-AI$^-$ at lower photon energies, as shown in Fig. 3. The near-threshold spectrum at the 2.7025 eV photon energy (Fig. 3(a)) yields a very accurate adiabatic detachment energy (ADE) or the electron affinity (EA) of 2.6967 ± 0.0008 eV (21 751 ± 6 cm^{-1}) for the 7-AI radical. The 2.8458 eV spectrum (Fig. 3(b)) resolves a number of weak vibrational peaks, labeled A through D. The binding energies and shifts relative to the 0–0 transition are given in Table S2, where they are compared with the computed vibrational frequencies for the 7-AI radical. The very weak $^{x}0_0^0$ signal due to the ^{x}7-AI$^-$ isomer is also observed in Fig. 3.

3.2. Photodetachment spectroscopy

The previous PDS study of 7-AI$^-$ by Noble *et al.* revealed a DBS, because the 7-AI radical possesses a dipole moment of 4.64 D,[28] higher than the 2.5 D critical value.[65] They observed a photodetachment threshold of 21 750 ± 10 cm^{-1} (2.697 eV), in excellent agreement with the EA of 21 751 ± 6 cm^{-1} (2.6967 eV) for the 7-AI radical measured in our PES experiment (Fig. 3). The binding energy of the DBS was measured to be 160 ± 10 cm^{-1} by Noble *et al.* In addition, they observed seven vibrational Feshbach resonances of the DBS in their reported spectral range ending at 22 700 cm^{-1}. However, assignments of the vibrational features were challenging. We have shown that resonant PES *via* the DBS can be used to assign the vibrational features on the basis of the $\Delta\nu = -1$ propensity rule for vibrational autodetachment.[66,67] Furthermore, resonant PES yields much richer vibrational information than conventional non-resonant PES.[39]

In the current work, we conducted a PDS study of 7-AI$^-$ with higher spectral resolution using a 0.1 nm scanning step size over a broader spectral range extending to 23 520 cm^{-1}, as shown in Fig. 4. In the same spectral range up to 22 700 cm^{-1}, the current spectrum agrees with that reported by Noble *et al.*:[27] the seven Feshbach resonances, labeled as 1, 4–6, 9, 10, and 13, were observed previously. Note that peak 13 is the most prominent resonance in the current PDS, whereas it was a very weak peak in the spectrum reported by Noble *et al.* We were also able to identify six weak resonances (peaks 2, 3, 7, 8, 11, 12) in this spectral range, which were not recognized previously. In addition, we observed three new Feshbach resonances, labeled as 14, 15, 16, at higher excitation energies beyond the spectral range reported by Noble *et al.* A sharp threshold is observed at

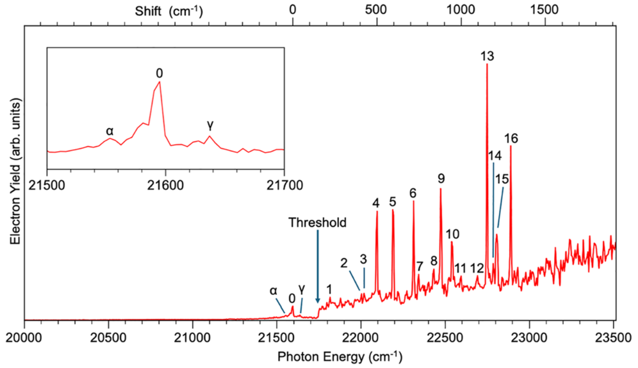

Fig. 4 Photodetachment spectroscopy of 7-AI$^-$. The top axis shows the energy shift relative to the DBS vibrational ground state, denoted as peak 0. The vibrational levels of the DBS (vibrational Feshbach resonances) are labeled as peaks 1–16. The inset provides an expanded view of the 21 500–21 700 cm^{-1} spectral region. The arrow at 21 751 cm^{-1} marks the detachment threshold.

21 751 cm^{-1}, matching exactly the EA of 7-AI determined from the high resolution PES (Fig. 3). The prompt onset at threshold suggests s-wave detachment according to the Wigner threshold law,[68] consistent with detachment from the π HOMO (Fig. 2). Below the detachment threshold, a distinct feature (peak 0) appears at 21 595 cm^{-1} (2.6774 eV), corresponding to the zero-point vibrational level of the DBS. The DBS binding energy is measured as 156 ± 5 cm^{-1} (0.0193 ± 0.0006 eV), slightly more accurate than the value of 160 ± 10 cm^{-1} reported by Noble *et al.*[27] The excitation energies and vibrational assignments of the DBS vibrational levels are summarized in Table S3.

Owing to improved signal-to-noise ratios, the current photodetachment spectrum reveals a broad background near peak 0, which disappears below ∼21 200 cm^{-1}. Within this broad background, two weak features (α and γ) are discernible (inset of Fig. 4). As will be discussed later, these signals arise from isomeric forms of 7-AI$^-$, as already hinted in the PE spectra (Fig. 1 and 3).

As we have shown previously, the DBS vibrational levels in general mirror the FC envelope of the ground state transition in non-resonant PES.[39] This is because the highly diffuse dipole-bound electron has little effect on the structure of the neutral core and the potential energy surface of the DBS is nearly identical to that of the neutral ground state. Fig. 1 shows that the FC envelope for the ground state transition (the $\tilde{X}$ band) spans an energy range of ∼0.6 eV. However, the Feshbach resonances in the photodetachment spectrum abruptly end at peak 16, only about 0.16 eV above the DBS zero-point level. According to the FC envelope of the PE spectra, we expected to observe extensive DBS vibrational peaks above peak 16 in the photodetachment spectrum, extending to at least 4800 cm^{-1}. We will show later that the abrupt loss of Feshbach resonances above peak 16 is likely due to the competition between autodetachment and relaxation to a nearby electronic excited state (shape resonance) of the 7-AI$^-$ anion.

3.3. R2PD photoelectron imaging

The bound zero-point level of the DBS (peak 0 in Fig. 4) is observed through the single-color R2PD process, where the first photon excites the anion to the DBS zero-point level and the second photon within the same 5 ns laser pulse detaches the diffuse DBS electron.[39,49] R2PD photoelectron imaging probes the nature of the DBS and relaxation processes that may occur within the duration of the laser pulse. Fig. 5 displays the single-color R2PD photoelectron image and spectrum at peak 0 in the PDS. Two major signals are observed, one at the low binding energy side (labeled as "DBS") and another at the high binding energy side (labeled as "S_0"). The "DBS" band at the low binding energy side originates from the expected sequential two-photon process. The low binding energy of this band, which could not be measured accurately due to its high electron kinetic energy, is consistent with the accurate measurement of 156 cm^{-1} (0.0193 eV) from the PDS (Fig. 4). The angular distribution of this band (the outermost ring in the PE image in Fig. 5) exhibits a distinct p-wave character with a β parameter of 1.33 ± 0.05, as expected from the s-like dipole-bound orbital. The signals at the high binding energy side ("S_0") should be due to detachment from vibrational levels of the ground state (S_0) of 7-AI$^-$, populated due to relaxation from the DBS zero-point level following the absorption of the first photon.[48,51,53] Four vibrational peaks (A_a–D_a) are resolved within the "S_0" signals; their binding energies, shifts from the 0–0 transition in the PE spectra of 7-AI$^-$, and their assignments are summarized in Table S4. The assignments are assisted with the computed frequencies of the 7-AI$^-$ anion (Fig. S2 and Table S5). The weak ${}^{x}0_0^0$ peak due to isomer ^{x}7-AI$^-$ is also observed in Fig. 5, similar to that in the PE spectra shown in Fig. 1 and 3. In addition, an even weaker feature is observed at ∼1.9 eV (peak ${}^{y}0_0^0$), which is attributed to a different isomer ^{y}7-AI$^-$ (Fig. S1).

We took PE spectra by tuning the detachment laser to photon energies corresponding to the weak signals observed in the PDS around peak 0, *i.e.* at positions of α and γ, as shown in Fig. S3. Notably, the low binding energy "DBS" signal observed in Fig. 5 disappeared, suggesting that the weak signals in the PDS around peak 0 are not related to the main isomer of 7-AI$^-$. However, the ${}^{x}0_0^0$ and ${}^{y}0_0^0$ signals are the same as those in Fig. 5, confirming that those weak signals in the PDS should come from different isomers of 7-AI$^-$, *i.e.*, most likely corresponding to above-threshold excited states (*i.e.*, shape resonances) of the ^{x}7-AI$^-$ and ^{y}7-AI$^-$ isomers. The sharp

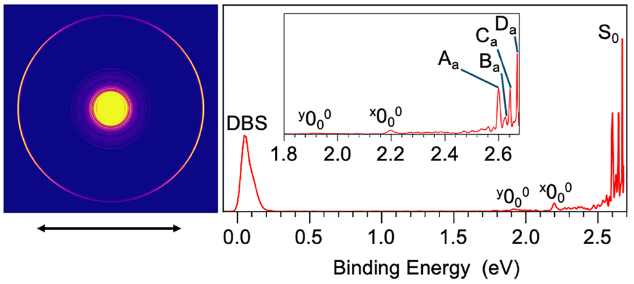

Fig. 5 One-color R2PD photoelectron image and spectrum of 7-AI$^-$ obtained at 2.6774 eV (corresponding to peak 0 in Fig. 4). The double arrow below the image indicates the laser polarization. The inset shows an expanded view of the high binding energy region.

peaks at the high binding energy side are probably due to autodetachment from the shape resonances from these isomers. We should emphasize that the ^{x}7-AI$^-$ and ^{y}7-AI$^-$ isomers were very weakly populated, only ∼1% compared to the main isomer. The resolved sharp peaks in the two spectra in Fig. S3 are different, indicating that the weak signals in the PDS probably consist of contributions from both isomers. The binding energies of the resolved features are given in Table S6. The ADEs of ^{x}7-AI$^-$ and ^{y}7-AI$^-$ measured from peaks $^{x}0_0^0$ and $^{y}0_0^0$ are 2.200 ± 0.003 eV and 1.918 ± 0.005 eV, respectively, which are compared with the calculated values in Table S7.

3.4. Resonant photoelectron imaging

Resonant PES *via* the Feshbach resonances yields highly non-Franck–Condon spectra due to the $\Delta v = -1$ propensity rule for vibrational autodetachment, allowing vibrational peaks with low FC factors or even FC-inactive vibrational modes in conventional PES to be significantly enhanced. Thus, rPES provides not only much richer spectroscopic information, but also a powerful means to assign the vibrational levels of the DBS. By tuning the detachment laser to the 16 Feshbach resonances observed in the PDS (Fig. 4), we obtained 16 resonant PE spectra, as shown in Fig. 6 and 7. Depending on the DBS levels accessed, certain vibrational peaks in the rPES become selectively enhanced, in comparison to the non-resonant PES shown in Fig. 3. More importantly, many new vibrational features are observed and they are labeled by lower case letters from a to j in Fig. 6 and 7. These newly observed vibrational features, along with their corresponding electron binding energies, relative shifts from the vibrational origin (0_0^0), and their assignments, are also given in Table S2.

4. Discussion

4.1. Non-resonant PES

4.1.1. PES at high photon energies. The three PES bands observed at 4.661 eV (Fig. 1(b)) are derived from electron detachment from the HOMO, HOMO−1, and HOMO−2 of 7-AI$^-$ (Fig. 2). The angular distributions of the three bands are consistent with the symmetries of the MOs. The assignment of these bands agrees qualitatively with the computed vertical excitation energies for the 7-AI radical (Table S1). Extensive vibrational features are resolved for the X̃ band in the 3.496 eV spectrum (Fig. 1(a)). Vibrational features are partially resolved for the X̃ band even in the 4.661 eV spectrum. However, no discernible vibrational features are resolved for the two weaker excited state bands, Ã and B̃. This observation suggests strong vibronic couplings among the low-lying excited states of the 7-AI radical, as observed previously in the smaller pyrrolyl radical or the isoelectronic indolyl radical.[47,69] In fact, the 4.661 eV spectrum of 7-AI$^-$ exhibits some similarities to that of pyrrolide at 4.3446 eV or in particular that of indolide. We also find that the valence MOs of 7-AI$^-$ are similar to those of the indolide anion.[47] The strong vibronic coupling among the

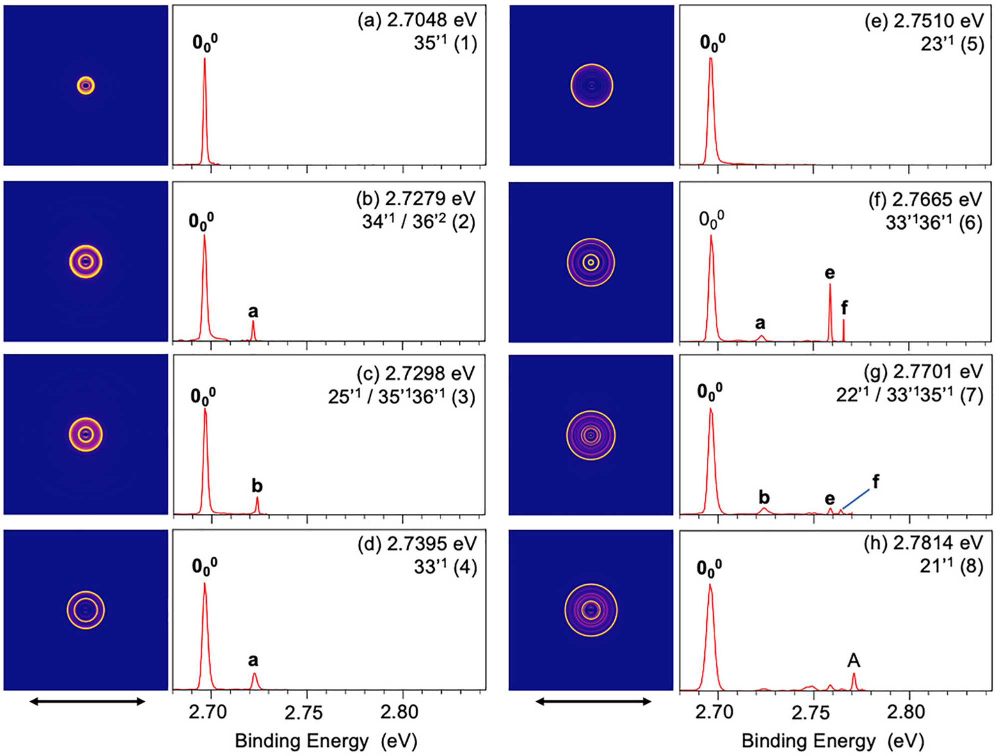

Fig. 6 Resonant PE images and spectra of 7-AI$^-$ at peaks 1–8 in the PDS (Fig. 4 and Table S3). (a) 2.7048 eV (21 816 cm^{-1}), (b) 2.7279 eV (22 002 cm^{-1}), (c) 2.7298 eV (22 018 cm^{-1}), (d) 2.7395 eV (22 096 cm^{-1}), (e) 2.7510 eV (22 188 cm^{-1}), (f) 2.7665 eV (22 314 cm^{-1}), (g) 2.7701 eV (22 343 cm^{-1}), (h) 2.7814 eV (22 434 cm^{-1}). The double arrow below the images represents the polarization direction of the laser.

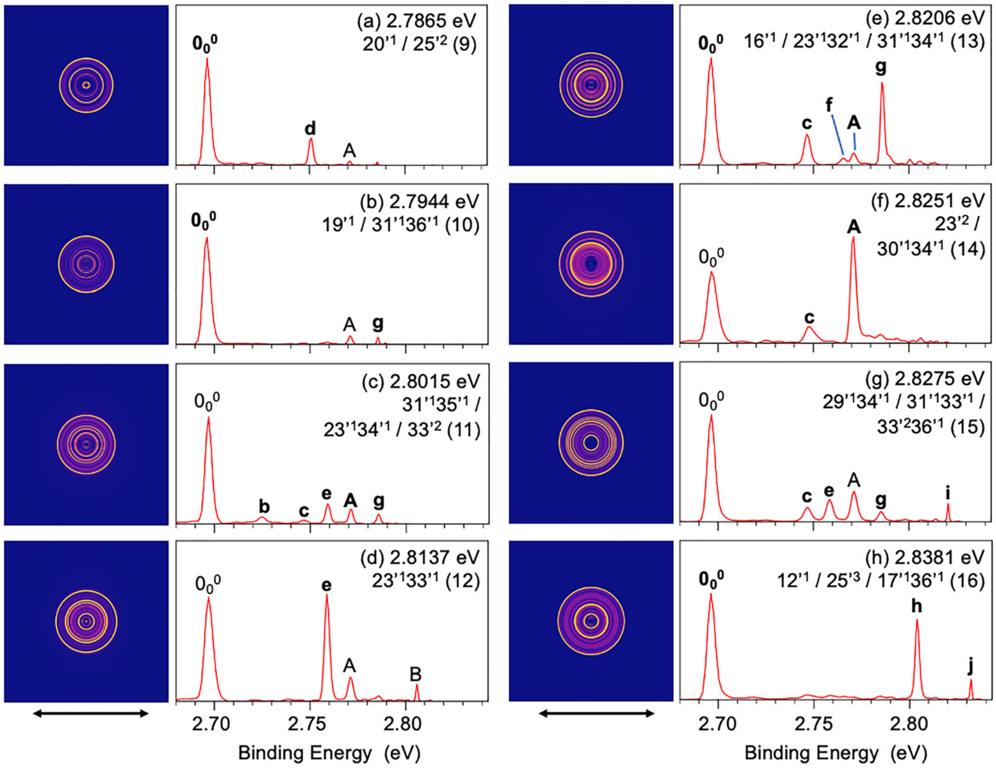

Fig. 7 Resonant PE images and spectra of 7-AI$^-$ at peaks 9–16 in the PDS (Fig. 4 and Table S3). (a) 2.7865 eV (22 475 cm^{-1}), (b) 2.7944 eV (22 539 cm^{-1}), (c) 2.8015 eV (22 596 cm^{-1}), (d) 2.8137 eV (22 694 cm^{-1}), (e) 2.8206 eV (22 750 cm^{-1}), (f) 2.8251 eV (22 786 cm^{-1}), (g) 2.8275 eV (22 806 cm^{-1}), (h) 2.8381 eV (22 891 cm^{-1}). The double arrow below the images represents the polarization direction of the laser.

low-lying states in 7-AI is probably one of the reasons that the computed excitation energies using TD-DFT are overestimated in comparison to the experimental observations (Table S1).

4.1.2. Franck–Condon simulation for the ground state detachment transition. To understand the vibrational features in the non-resonant PE spectra, we calculated the FC factors for the ground state detachment transition using the computed harmonic vibrational frequencies for the neutral final states (Table S8 and Fig. S4). The computed FC factors are compared with the high-resolution PE spectrum at 2.8458 eV in Fig. 8 and the high photon energy spectra in Fig. S5. The agreement between the computed FC factors and the overall $\tilde{X}$ band shape at 4.661 eV is reasonable, although the FC profile of the 3.496 eV spectrum is anomalous with increasing intensity on the higher binding energy side. As will be shown below, the 7-AI$^-$ anion has a valence excited state near this photon energy, which may distort the PE spectrum due to autodetachment. Owing to the planar geometry (C_s) of both the 7-AI$^-$ anion and the 7-AI neutral radical, only in-plane vibrational modes (A$'$ symmetry) are symmetry-allowed. The calculated FC factors agree well with the observed vibrational features in the low binding energy region probed at the 2.8458 eV photon energy (Fig. 8). Peaks A, B, C, and D are due to the ν_{23}, ν_{20}, ν_{19}, and ν_{16} modes (Table S2), respectively, on the basis of the computed harmonic frequencies. The good agreement is expected because the low photon energy at 2.8458 eV only probes the potential energy surface near the equilibrium of the 7-AI ground state. The higher energy part accessed at high photon energies (Fig. S5) is expected to deviate from the FC calculations due to the vibronic coupling of the ground state with the excited states, as observed in similar molecular systems previously.[47,69]

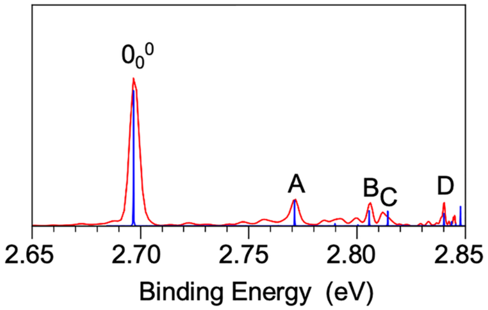

Fig. 8 The PE spectrum of 7-AI$^-$ at 2.8458 eV compared with the calculated FC factors. The vibrational frequencies of neutral 7-AI computed at the B3LYP level are scaled by a factor of 0.98 (Table S8).

4.1.3. Isomers of 7-AI$^-$. We have evidence for a minor isomer of 7-AI$^-$ from the PES data in Fig. 1 and 3, designated as ^{x}7-AI$^-$ with a measured ADE of 2.200 eV. The weak signals in the PDS near peak 0 (Fig. 4) also suggest the existence of lower binding energy isomers. The R2PD PE spectrum at 2.6774 eV in Fig. 5 not only confirms the existence of the ^{x}7-AI$^-$ isomer, but also reveals another even weaker isomer (^{y}7-AI$^-$) with a lower measured ADE of 1.918 eV. In our previous high-resolution PES study on the pyrrolide anion (Py$^-$),[69] which constitutes the 5-membered ring of the 7-AI$^-$ anion, we observed a weak isomer due to deprotonation from the α-carbon ($^{\alpha}$Py$^-$). The ADE of Py$^-$ was measured to be 2.1433 eV, whereas that of $^{\alpha}$Py$^-$ was measured to be smaller by 0.4743 eV at 1.6690 eV.[69] We note that the ADE of the ^{x}7-AI$^-$ isomer (2.200 eV) is also smaller than that of 7-AI$^-$ (2.6967 eV) by about the same amount (0.4967 eV), suggesting that the isomer ^{x}7-AI$^-$ is likely due to deprotonation at the same α-carbon position on the pyrrole ring as shown in Fig. S1. The computed ADE of ^{x}7-AI$^-$ is 2.17 eV (Table S7), in excellent agreement with the experimental value of 2.200 eV. There is strain on the 5-memebered ring, making the H atom on the α-carbon more acidic. We computed the ADE for another isomer, in which the β-carbon on the pyrrole ring in 7-AI$^-$ is deprotonated (Fig. S1), and found it to be 1.79 eV, consistent with the measured ADE of 1.918 eV for isomer ^{y}7-AI$^-$ (Table S7). We also considered isomers with deprotonation on the pyridine ring of 7-AI$^-$ and found that their ADEs are all much smaller. Thus, the ^{y}7-AI$^-$ isomer should be due to deprotonation on the β-carbon of the pyrrole ring. We should point out that the populations of isomers ^{x}7-AI$^-$ and ^{y}7-AI$^-$ are very small. The fact that we are able to detect these weak isomers at all is a testimony of the effectiveness of cryogenic cooling and the sensitivity of our experiment. While these isomers may be interesting in their own right, their weak populations prevent us from studying their spectroscopy in detail.

4.2. Comparison between PDS and non-resonant PES

The photodetachment spectrum of 7-AI$^-$ (Fig. 4) exhibits a series of resonances associated with the vibrational levels of the DBS. The weak below-threshold feature at 21 595 cm^{-1} (2.6774 eV) (peak 0) is the zero-point level of the DBS with a binding energy of 156 ± 5 cm^{-1}. Because the 156 cm^{-1} DBS binding energy is lower than the lowest vibrational frequency of neutral 7-AI (Fig. S4 and Table S8), any vibrational excitation of the DBS would be above the detachment threshold, which can result in vibrational autodetachment. The DBS origin is observed through R2PD processes, whereas the Feshbach resonances (peaks 1–16) are observed due to single photon excitation, followed by vibrational autodetachment, during which vibrational energy is transferred to the dipole-bound electron. The diffuse dipole-bound electron has negligible perturbation to the geometry of neutral 7-AI, such that the vibrational structures of the DBS mirror those of the neutral final state observed in the PES.[39] This similarity is evident in Fig. S6, where the PD spectrum is overlaid on the high resolution PE spectrum at 2.8458 eV by aligning peak 0 (the DBS origin) with the 0–0 transition in the PE spectrum. The vibrational transitions observed in the PE spectrum have clear counterparts in the PD spectrum, allowing those DBS vibrational levels to be readily assigned. In general, much more vibrational features are observed in PDS because of the much higher cross sections in the resonant excitation. Thus, PDS can be viewed as "electron-tagging" vibrational spectroscopy of the neutral radicals *via* the DBS,[49] with the caveat that the observed DBS features are governed by vibrational autodetachment.

The comparison between the PES and PDS (Fig. S6) shows that the PES peaks A, B, C, and D align with the PDS peaks 5, 9, 10, and 13, respectively. Following the assignment of the PES peaks from the FC simulation (Fig. 8 and Table S2), the PDS peaks can be immediately assigned to $23'^1$, $20'^1$, $19'^1$, and $16'^1$,[1] respectively (the $'$ sign is used to designate DBS levels). Notably, more vibrational resonances are present in the PD spectrum, *e.g.* the intense peaks 4 and 6, as well as several very weak peaks (*i.e.*, 2, 3, 7, 8, 11, and 12), which do not have counterparts in the PES. These resonances likely involve vibrational modes with weak FC factors or symmetry-forbidden transitions. They become accessible under resonant excitation conditions in PDS, illustrating the sensitivity of PDS and its power to yield richer vibrational information. Assignment of these DBS resonances can be done using rPES on the basis of the $\Delta\nu = -1$ vibrational autodetachment propensity rule,[66,67] and the computed vibrational frequencies for neutral 7-AI (Table S8). Not only is the rPES powerful to reveal the nature of the observed DBS vibrational peaks, but it also often uncovers overlapping DBS vibrational levels which give rise to complicated PES features with new vibrational final states not accessible in non-resonant PES.

The FC simulation (Fig. S5) confirms the broad FC profile for the ground state detachment transition. However, the DBS vibrational features appear only in a narrow energy range above threshold and end abruptly at peak 16 (Fig. 4), suggesting other processes may compete with vibrational autodetachment beyond peak 16. We computed the first excited state for the 7-AI$^-$ anion at the B3LYP level and found that both S_1 and T_1 occur around 2.81 eV (Table S9), near peak 16, which has an excitation energy of 2.8381 eV (Table S3). Our computed excitation energy for S_1 is consistent with the 2.98 eV excitation energy calculated by Noble *et al.* at the CAM-B3LYP level.[28] The S_1 of 7-AI$^-$ should be a broad shape resonance. Thus, two competing processes may happen for the Feshbach resonances above peak 16: (1) autodetachment; and (2) relaxation to S_1. The autodetachment lifetime is known to be on the order of a few to few tens of picosecond,[70] whereas the relaxation to the S_1 could occur on much faster time scale,[71] which would prevent the Feshbach resonances from being observed. While not explicitly recognized, such a competition between the Feshbach resonances and shape resonance was actually present in the 1-pyrenolate anion reported previously,[43] resulting in a short DBS vibrational profile in its PDS, compared to the PES data.

4.3. Resonant photoelectron images and spectra

The rPES images and spectra in Fig. 6 and 7 consist of two distinct electron detachment processes: (1) direct photodetachment from the anion ground state to that of the neutral final states and (2) autodetachment from specific vibrational levels of the DBS. Because of the structural similarity between the DBS of 7-AI$^-$ and the neutral 7-AI, autodetachment follows the $\Delta\nu = -1$ propensity rule under the harmonic approximation.[66,67] If a vibrational level $v_x'^n$ of the DBS is excited, the

ν_x^{n-1} vibrational level of the neutral will be enhanced due to the coupling of one vibrational quantum to the weakly-bound electron during autodetachment. For combinational levels involving multiple vibrational modes, *e.g.*, $\mathrm{v}_x'^{n}\mathrm{v}_y'^{m}$, multiple neutral vibrational levels, *i.e*, $\nu_x^{n-1}\nu_y^{m}$ or $\nu_x^{n}\nu_y^{m-1}$ may be enhanced. Thus, rPES is highly non-Franck–Condon, because vibrational final states with weak FC factors or even FC-inactive modes can be significantly enhanced. Thus, in addition to providing rich vibrational information for the neutral final state, rPES serves as a powerful tool to assist the assignment of the Feshbach resonances observed in PDS. The normal modes of vibration for neutral 7-AI are shown in Fig. S4. The computed frequencies scaled by a factor of 0.98 are given in Table S8.

4.3.1. Resonant PES at vibrational peaks 1–8 of the DBS. At low excitation energies, the resonant PE spectra are relatively simple and straightforward to understand. Peaks 1, 5, and 8 in the PDS correspond to excitation to the $35'^{1}$, $23'^{1}$, and $21'^{1}$ DBS vibrational levels, respectively. The resulting resonant PE spectra in Fig. 6(a), (e), and (h) all exhibit an enhanced 0_0^0 transition, according to the $\Delta\nu = -1$ propensity rule. Fig. 6(b) pertains to excitation of an overlapping DBS level: $34'^{1}$, which led to an enhanced 0_0^0 transition, and the $36'^{2}$ overtone, which gave rise to a new weak peak a (36^1). Fig. 6(c) also arises from excitation of an overlapping DBS level: $25'^{1}$ and the $35'^{1}36'^{1}$ combinational level, resulting in the enhancement of the 0_0^0 transition and a new weak peak b (35^1). In the latter case, the v_{36}' mode couples more strongly with the dipole-bound electron, causing the appearance of peak b (35^1). Such mode selectivity was observed in the first rPES done on the phenoxide anion[33] and was quantitatively investigated using pump–probe experiment.[70] The strong DBS peak 4 at an excitation energy of 501 cm^{-1} (Table S3) corresponds to $33'^{1}$, resulting in the enhanced 0_0^0 transition (Fig. 6(d)). However, peak a unexpectedly appeared, corresponding to excitation of the lowest frequency mode of the neutral 7-AI final state (36^1, Table S2). The appearance of this peak could be due to inelastic scattering or threshold effect as a result of vibronic coupling.[72,73] The strong resonant peak 6 is from excitation to the $33'^{1}36'^{1}$ combinational level of the DBS, yielding two new PES peaks a (36^1) and e (33^1) (Fig. 6(f)), as expected from $\Delta\nu = -1$ autodetachment processes. The weak peak f (32^1) right at threshold is likely due to a threshold effect and vibronic coupling. Fig. 6(g) comes from excitation of an overlapping DBS level: $22'^{1}$, resulting in the enhanced 0_0^0 transition and the $33'^{1}35'^{1}$ combinational level, giving rise to the weak b (35^1) and e (33^1) final states (Fig. 6(g)). The appearance of peak f in Fig. 6(g) is probably due to the same reason as that in Fig. 6(f) because the resonances 6 and 7 are very close to each other.

4.3.2. Resonant PES at vibrational peaks 9–16 of the DBS. At higher excitation energies, overlapping DBS levels are more likely because of the increased vibrational density of states, resulting in more complicated rPES features, as shown in Fig. 7. The resonant peaks 9 and 10 correspond to the FC-allowed PES peaks B (20^1) and C (19^1) (Fig. S6), respectively. Thus, they should correspond to the $20'^{1}$ and $19'^{1}$ DBS levels, respectively, resulting in the enhanced 0_0^0 transition in Fig. 7(a) and (b). The new peak d (25^1) in Fig. 7(a) indicates that the DBS resonant peak 9 contains an overlapping $25'^{2}$ level, and the new peak g (31^1) in Fig. 7(b) suggests an overlapping level of $31'^{1}36'^{1}$. All the new peaks (a, b, d, e, f, g) (Table S2) appearing in the rPES are symmetry-forbidden or FC-inactive in the non-resonant PES (Fig. 3(b)). The weak resonant peak 11 gives rise to one of the most complicated resonant PE spectra with four new final state peaks, b (35^1), c (34^1), e (33^1), and g (31^1) (Fig. 7(c)). These rPES vibrational features for the neutral 7-AI radical come from three overlapping DBS vibrational levels ***via*** $\Delta\nu = -1$ autodetachment: $31'^{1}35'^{1}/23'^{1}34'^{1}/33'^{2}$, which all have excitation energies around 1000 cm^{-1} above the zero-point level of the DBS (Table S3). The weak resonant peak 12 due to excitation of the $23'^{1}33'^{1}$ DBS level produces a remarkable resonant PE spectrum with an intense peak e (33^1). Apparently, the v_{23}' mode is selectively coupled with the dipole-bound electron to induce autodetachment, whereas the coupling of the v_{33}' mode is weak. The resonant peak 13 represents the strongest transition in the PDS (Fig. 4), corresponding to the FC-active v_{16}' mode (Fig. S5). Thus, we expect a strongly enhanced 0–0 transition in the rPES (Fig. 7(e)). However, three new peaks are observed in the rPES, c (34^1), f (32^1), and g (31^1). The intense peaks c and g indicate that excitation to the $31'^{1}34'^{1}$ combinational DBS level makes a strong contribution to peak 13. The observation of weak peak f suggests that excitation to the $23'^{1}32'^{1}$ combinational DBS level also contributes slightly to peak 13.

The weak resonant peak 14 also produces a remarkable resonant PE spectrum with a hugely enhanced peak A (Fig. 7(f)), suggesting that peak 14 is mainly due to excitation to the $\nu = 2$ level of the FC-active v_{23}' mode in the DBS. The appearance of peak c (34^1) suggests that the $30'^{1}34'^{1}$ combinational DBS level also contributes to peak 14. The resonant peak 15 gives rise to a complicated resonant PE spectrum with four new peaks, c (34^1), e (33^1), g (31^1), and i (33^2) (Fig. 7(g) and Table S2). These new rPES features come from autodetachment from three overlapping vibrational levels contained in peak 15: $29'^{1}34'^{1}/31'^{1}33'^{1}/33'^{2}36'^{1}$, which all have excitation energies around 1200 cm^{-1} above the DBS zero-point level (Table S3). Finally, a simple resonant PE spectrum (Fig. 7(h)) is observed at the resonant peak 16 with a strongly enhanced 0_0^0 transition due to excitation of the $12'^{1}$ DBS level. The strong peak h (25^2) has to come from an overlapping $25'^{3}$ DBS level, which has an excitation energy nearly identical as that of $12'^{1}$ (Table S3). The relatively weak peak j (17^1) in Fig. 7(h) suggests that excitation of the $17'^{1}36'^{1}$ DBS level also contributes to the resonant peak 16.

4.4. Vibrational information obtained for the 7-AI radical

Fig. 9 displays the vibrational levels observed for neutral 7-AI and autodetachment from selected DBS vibrational levels. Note that many more vibrational features (a–j) come from rPES. The relaxation from the DBS to the anion excited state (shape

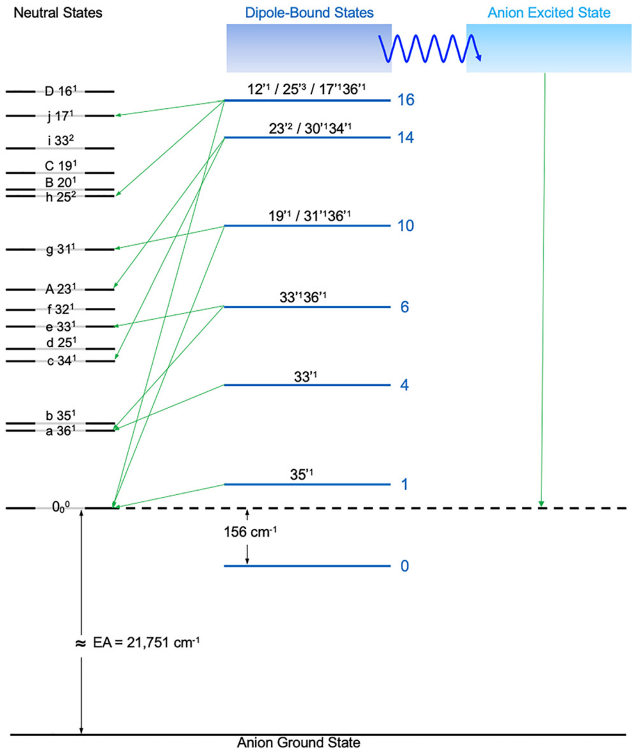

Fig. 9 Schematic diagram showing the observed vibrational levels for neutral 7-AI and autodetachment from a few selected DBS vibrational Feshbach resonances of 7-AI$^-$. See Table S3 for the assignment of all the 16 observed Feshbach resonances. The relaxation from the DBS to the putative valence excited state of 7-AI$^-$ is also shown schematically.

resonance) at higher excitation energies is also schematically shown, explaining why the DBS resonances end abruptly above peak 16 in the PDS (Fig. 4).

The rich vibrational information obtained from the resonant PE spectra shown in Fig. 6 and 7 illustrates the potential of rPES, in comparison with conventional PES. Not only can vibrational transitions with weak FC factors be significantly enhanced, even symmetry-forbidden transitions or transitions with negligible FC factors can be observed in rPES. Furthermore, PDS provides additional and complementary vibrational information about the neutral final states, because the dipole-bound electron has negligible influence on the neutral geometry. In fact, PDS often yields more accurate vibrational information, because the resolution of PEI depends on the kinetic energies of the photoelectrons. For the 7-AI radical, the high resolution PES in Fig. 3 only reveal four vibrational peaks, A, B, C, D, corresponding to the FC-active ν_{23}, ν_{20}, ν_{19}, and ν_{16} modes of 7-AI, respectively. However, the rPES data yield 10 additional vibrational peaks, a to j (Table S2), most of which are symmetry-forbidden bending modes. Combining the PES, rPES, and PDS data, we obtain 16 experimental vibrational frequencies for the 7-AI radical, as given in Table 1, along with the calculated frequencies. We found that the computed frequencies at the B3LYP level are in good agreement with the experimental data with a scaling factor of 0.98.[74]

Table 1 Fundamental vibrational frequencies measured for the 7-AI radical, compared with theoretical values computed at the B3LYP/aug-cc-pVTZ level

Vibrational mode	Symmetry	Experimental frequency^a (cm^{-1})	Theoretical frequency^b (cm^{-1})
ν_{12}	A′	1296(5)	1304
ν_{16}		1155(5)	1156
ν_{17}		1092(6)	1089
ν_{19}		944(5)	947
ν_{20}		880(5)	878
ν_{21}		839(5)	836
ν_{22}		748(5)	751
ν_{23}		593(5)	600
ν_{25}		423(5)	435
ν_{26}	A″	1000(6)	975
ν_{31}		717(8)	728
ν_{32}		550(6)	561
ν_{33}		501(5)	502
ν_{34}		407(5)	413
ν_{35}		221(5)	232
ν_{36}		210(9)	219

[a] The numbers in parentheses denote the uncertainty associated with the last digit. [b] The calculated shift is scaled by a factor of 0.98.

5. Conclusion

In conclusion, we report an investigation of the cryogenically-cooled 7-azaindolide anion (7-AI$^-$) using high-resolution photoelectron imaging in combination with photodetachment spectroscopy and resonant photoelectron spectroscopy. The electron affinity of the 7-AI radical is measured accurately to be 2.6967(8) eV (21 751 ± 6 cm^{-1}). Two low-lying electronic excited states of the neutral radical are identified at ∼0.8 eV and ∼1.4 eV above the ground state with evidence of strong vibronic coupling. Two minor isomers of the 7-AI$^-$ anions are also observed with lower adiabatic detachment energies measured at 2.200(3) eV and 1.918(5) eV, corresponding to deprotonation at the α- and β-carbon of 7-AI$^-$, respectively. A dipole-bound state is observed at 156 cm^{-1} below the detachment threshold of 7-AI$^-$, along with 16 vibrational Feshbach resonances. The resonant two-photon photoelectron spectrum obtained *via* the zero-point level reveals a relatively long-lived DBS, while relaxation to the ground state of the anion is also observed within the 5 ns duration of the detachment laser. Resonant photoelectron spectroscopy was conducted *via* the 16 vibrational levels of the DBS, revealing rich spectral features not accessible in conventional PES. The resonant PES was further used to confirm the assignment of the Feshbach resonances based on the $\Delta\nu = -1$ autodetachment propensity rule. The combination of PES, PDS, and rPES establishes vibrational frequencies for sixteen fundamental modes of the 7-AI radical. The electronic and vibrational spectroscopic information provides new benchmarks for further theoretical studies of this important radical species.

Author contributions

J. K. did the experiment, analyzed the data and wrote the first draft of the manuscript. E. I. B. assisted with the experiment. L.

S. W. guided and advised the project and revised and finalized the manuscript.

Conflicts of interest

The authors declare no conflict of interest.

Data availability

The data that supports the findings of this study is available from the corresponding author upon request.

Supplementary information is available. See DOI: **https://doi.org/10.1039/d5cp04123f**.

Acknowledgements

We would like to thank Dr Yue-Rou Zhang and Dr Dao-Fu Yuan for their invaluable experimental expertise. This work was supported by the U.S. Department of Energy, Office of Basic Energy Sciences, Chemical Sciences, Geosciences, and Biosciences Division under Grant No. DE-SC0018679. The calculations were conducted using computational resources and services at the Center for Computation and Visualization (CCV), Brown University.

References

1 Y. Chen, R. L. Rich, F. Gai and J. W. Petrich, *J. Phys. Chem.*, 1993, **97**, 1770–1778.
2 Y. Huang, S. Arnold and M. Sulkes, *J. Phys. Chem.*, 1996, **100**, 4734–4738.
3 A. V. Smirnov, D. S. English, R. L. Rich, J. Lane, L. Teyton, A. W. Schwabacher, S. Luo, R. W. Thornburg and J. W. Petrich, *J. Phys. Chem. B*, 1997, **101**, 2758–2769.
4 A. Nakajima, M. Hirano, R. Hasumi, K. Kaya, H. Watanabe, C. C. Carter, J. M. Williamson and T. A. Miller, *J. Phys. Chem. A*, 1997, **101**, 392–398.
5 A. Nakajima, Y. Negishi, R. Hasumi and K. Kaya, *Eur. Phys. J. D*, 1999, **9**, 303–307.
6 L. Serrano-Andres, M. Merchan, A. C. Borin and J. Stalring, *Int. J. Quant. Chem.*, 2001, **84**, 181–191.
7 C. Kang, J. T. Yi and D. W. Pratt, *J. Chem. Phys.*, 2005, **123**, 094306.
8 Y. Koizumi, C. Jouvet, T. Norihiro, S. Ishiuchi, C. Dedonder-Lardeux and M. Fujii, *J. Chem. Phys.*, 2008, **129**, 104311.
9 K. Sakota, N. Komure, W. Ishikawa and H. Sekiya, *J. Chem. Phys.*, 2009, **130**, 224307.
10 M. Mukherjee, B. Bandyopadhyay and T. Chakraborty, *Chem. Phys. Lett.*, 2012, **546**, 74–79.
11 B. Marchetti, T. N. V. Karsili, M. N. R. Ashfold and W. Domcke, *Phys. Chem. Chem. Phys.*, 2016, **18**, 20007–20027.
12 I. Lamas, R. Montero, V. Martínez-Martínez, A. Longarte and L. Blancafort, *Phys. Chem. Chem. Phys.*, 2020, **22**, 18639–18645.
13 D. P. Chong, *Molecules*, 2021, **26**, 1947.
14 I. Lamas, R. Montero, V. Martínez-Martínez and A. Longarte, *Phys. Chem. Chem. Phys.*, 2024, **26**, 3240–3252.
15 C. A. Taylor, M. A. El-Bayoumi and M. Kasha, *Proc. Natl. Acad. Sci. U. S. A.*, 1969, **63**, 253–260.
16 A. Douhal, S. K. Kim and A. H. Zewail, *Nature*, 1995, **378**, 260–263.
17 P. T. Chou, W. S. Yu, Y. C. Chen, C. Y. Wei and S. S. Martinez, *J. Am. Chem. Soc.*, 1998, **120**, 12927–12934.
18 M. Chachisvilis, T. Fiebig, A. Douhal and A. H. Zewail, *J. Phys. Chem. A*, 1998, **102**, 669–673.
19 D. E. Folmer, E. S. Wisniewski, S. M. Hurley and A. W. Castleman, *Proc. Natl. Acad. Sci. U. S. A.*, 1999, **96**, 12980–12986.
20 T. Fiebig, M. Chachisvilis, M. Manger, A. H. Zewail, A. Douhal, I. Garcia-Ochoa and A. de La Hoz Ayuso, *J. Phys. Chem. A*, 1999, **103**, 7419–7431.
21 H. Y. Chen and I. Chao, *ChemPhysChem*, 2004, **5**, 1855–1863.
22 J. Catalan, P. Perez, J. C. del Valle, J. L. G. de Paz and M. Kasha, *Proc. Natl. Acad. Sci. U. S. A.*, 2004, **101**, 419–422.
23 O. H. Kwon and A. H. Zewail, *Proc. Natl. Acad. Sci. U. S. A.*, 2007, **104**, 8703–8708.
24 H. Sekiya and K. Sakota, *J. Photochem. Photobiol., C*, 2008, **9**, 81–91.
25 K. Fuke and H. Ishikawa, *Chem. Phys. Lett.*, 2015, **623**, 117–129.
26 W. C. Lineberger, *Ann. Rev. Phys. Chem.*, 2013, **64**, 21–36.
27 A. M. de Oliveira, PhD thesis, University of Colorado, 2018.
28 J. A. Noble, E. Marceca, C. Dedonder and C. Jouvet, *Phys. Chem. Chem. Phys.*, 2020, **22**, 27290–27299.
29 C. Hock, J. B. Kim, M. L. Weichman, T. I. Yacovitch and D. M. Neumark, *J. Chem. Phys.*, 2012, **137**, 244201.
30 I. Leon, Z. Yang and L. S. Wang, *J. Chem. Phys.*, 2013, **138**, 184304.
31 M. L. Weichman and D. M. Neumark, *Annu. Rev. Phys. Chem.*, 2018, **69**, 101–124.
32 D. L. Huang, P. D. Dau, H. T. Liu and L. S. Wang, *J. Chem. Phys.*, 2014, **140**, 224315.
33 H. T. Liu, C. G. Ning, D. L. Huang, P. D. Dau and L. S. Wang, *Angew. Chem., Int. Ed.*, 2013, **52**, 8976–8979.
34 H. T. Liu, C. G. Ning, D. L. Huang and L. S. Wang, *Angew. Chem., Int. Ed.*, 2014, **53**, 2464–2468.
35 G. Z. Zhu, C. H. Qian and L. S. Wang, *J. Chem. Phys.*, 2018, **149**, 164301.
36 D. L. Huang, H. T. Liu, C. G. Ning and L. S. Wang, *J. Chem. Phys.*, 2015, **142**, 124309.
37 D. L. Huang, C. G. Ning, H. T. Liu and L. S. Wang, *J. Phys. Chem. Lett.*, 2015, **6**, 2153–2157.
38 G. Z. Zhu, D. H. Huang and L. S. Wang, *J. Chem. Phys.*, 2017, **147**, 013910.
39 G. Z. Zhu and L. S. Wang, *Chem. Sci.*, 2019, **10**, 9409–9423.
40 C. H. Qian, G. Z. Zhu, Y. R. Zhang and L. S. Wang, *J. Chem. Phys.*, 2020, **152**, 214307.
41 D. F. Yuan, Y. Liu, C. H. Qian, Y. R. Zhang, B. M. Rubenstein and L. S. Wang, *Phys. Rev. Lett.*, 2020, **125**, 073003.
42 D. F. Yuan, Y. Liu, C. H. Qian, G. S. Kocheril, Y. R. Zhang, B. M. Rubenstein and L. S. Wang, *J. Phys. Chem. Lett.*, 2020, **11**, 7914–7919.

43 C. H. Qian, Y. R. Zhang, D. F. Yuan and L. S. Wang, *J. Chem. Phys.*, 2021, **154**, 094308.

44 D. F. Yuan, Y. R. Zhang, C. H. Qian, Y. Liu and L. S. Wang, *J. Phys. Chem. A*, 2021, **125**, 2967–2976.

45 Y. R. Zhang, D. F. Yuan and L. S. Wang, *J. Am. Chem. Soc.*, 2022, **144**, 16620–16630.

46 Y. R. Zhang, D. F. Yuan and L. S. Wang, *J. Phys. Chem. Lett.*, 2022, **13**, 11481–11488.

47 D. F. Yuan, Y. Liu, Y. R. Zhang and L. S. Wang, *J. Am. Chem. Soc.*, 2023, **145**, 5512–5522.

48 Y. R. Zhang, D. F. Yuan, C. H. Qian, G. Z. Zhu and L. S. Wang, *J. Am. Chem. Soc.*, 2023, **145**, 14952–14962.

49 Y. R. Zhang, D. F. Yuan and L. S. Wang, *J. Phys. Chem. Lett.*, 2023, **14**, 7368–7381.

50 J. Kang, E. I. Brewer, D. F. Yuan, Y. R. Zhang and L. S. Wang, *J. Phys. Chem. A*, 2025, **129**, 1060–1067.

51 J. Kang and L. S. Wang, *J. Phys. Chem. A*, 2025, **129**, 8828–8836.

52 G. Z. Zhu, L. F. Cheung, Y. Liu, C. H. Qian and L. S. Wang, *J. Phys. Chem. Lett.*, 2019, **10**, 4339–4344.

53 Y. R. Zhang, D. F. Yuan, C. H. Qian and L. S. Wang, *J. Chem. Phys.*, 2021, **155**, 124305.

54 D. F. Yuan, Y. R. Zhang, C. H. Qian and L. S. Wang, *Phys. Chem. Chem. Phys.*, 2022, **24**, 1380–1389.

55 J. Kang, E. I. Brewer, Y. R. Zhang, D. F. Yuan, G. S. Kocheril and L. S. Wang, *J. Chem. Phys.*, 2024, **160**, 184301.

56 J. Kang, E. I. Brewer, Y. R. Zhang, D. F. Yuan, S. C. Tian, W. Roberts and L. S. Wang, *J. Chem. Phys.*, 2025, **162**, 194302.

57 L. S. Wang, *J. Chem. Phys.*, 2015, **143**, 040901.

58 L. S. Wang, C. F. Ding, X. B. Wang and S. E. Barlow, *Rev. Sci. Instrum.*, 1999, **70**, 1957–1966.

59 X. B. Wang and L. S. Wang, *Rev. Sci. Instrum.*, 2008, **79**, 073108.

60 I. Leon, Z. Yang, H. T. Liu and L. S. Wang, *Rev. Sci. Instrum.*, 2014, **85**, 083106.

61 B. Dick, *Phys. Chem. Chem. Phys.*, 2019, **21**, 19499–19512.

62 J. Cooper and R. N. Zare, *J. Chem. Phys.*, 1968, **48**, 942–943.

63 M. J. Frisch, G. W. Trucks, H. B. Schlegel, G. E. Scuseria, M. A. Robb, J. R. Cheeseman, G. Scalmani, V. Barone, G. A. Petersson, H. Nakatsuji, X. Li, M. Caricato, A. Marenich, J. Bloino, B. G. Janesko, R. Gomperts, B. Mennucci, H. P. Hratchian, J. V. Ortiz, A. F. Izmaylov, J. L. Sonnenberg, D. Williams-Young, F. Ding, F. Lipparini, F. Egidi, J. Goings, B. Peng, A. Petrone, T. Henderson, D. Ranasinghe, V. G. Zakrzewski, J. Gao, N. Rega, G. Zheng, W. Liang, M. Hada, M. Ehara, K. Toyota, R. Fukuda, J. Hasegawa, M. Ishida, T. Nakajima, Y. Honda, O. Kitao, H. Nakai, T. Vreven, K. Throssell, J. A. Montgomery, Jr., J. E. Peralta, F. Ogliaro, M. Bearpark, J. J. Heyd, E. Brothers, K. N. Kudin, V. N. Staroverov, T. Keith, R. Kobayashi, J. Normand, K. Raghavachari, A. Rendell, J. C. Burant, S. S. Iyengar, J. Tomasi, M. Cossi, J. M. Millam, M. Klene, C. Adamo, R. Cammi, J. W. Ochterski, R. L. Martin, K. Morokuma, O. Farkas, J. B. Foresman and D. J. Fox, *Gaussian 09, Revision D.01*, Gaussian, Inc., Wallingford CT, 2016.

64 I. Pugliesi and K. Müller-Dethlefs, *J. Phys. Chem. A*, 2006, **110**, 4657–4667.

65 C. H. Qian, G. Z. Zhu and L. S. Wang, *J. Phys. Chem. Lett.*, 2019, **10**, 6472–6477.

66 R. S. Berry, *J. Chem. Phys.*, 1966, **45**, 1228–1245.

67 J. Simons, *J. Am. Chem. Soc.*, 1981, **103**, 3971–3976.

68 E. P. Wigner, *Phys. Rev.*, 1948, **73**, 1002–1009.

69 Y. R. Zhang, D. F. Yuan and L. S. Wang, *Phys. Chem. Chem. Phys.*, 2022, **24**, 6505–6514.

70 D. H. Kang, S. An and S. K. Kim, *Phys. Rev. Lett.*, 2020, **125**, 093001.

71 C. J. Clarke and J. R. R. Verlet, *Annu. Rev. Phys. Chem.*, 2024, **75**, 89–110.

72 D. L. Huang, H. T. Liu, C. G. Ning, P. D. Dau and L. S. Wang, *Chem. Phys.*, 2017, **482**, 374–383.

73 H. W. Gao, J. Hui and L. S. Wang, *J. Phys. Chem. Lett.*, 2025, **16**, 2039–2046.

74 P. Sinha, S. E. Boesch, C. Gu, R. A. Wheeler and A. K. Wilson, *J. Phys. Chem. A*, 2004, **108**, 9213–9217.